Additive manufacturing of interstitial-strengthened high entropy alloy: Scanning strategy dependent anisotropic mechanical properties

Zhang, Wei; Wang, Hui; Kooi, Bart; Pei, Yutao

Published in:
Materials science and engineering a-Structural materials properties microstructure and processing

DOI:
10.1016/j.msea.2023.144978

Publication date:
2023

Materials Science & Engineering A 872 (2023) 144978

Contents lists available at ScienceDirect

Materials Science & Engineering A

journal homepage: www.elsevier.com/locate/msea

Additive manufacturing of interstitial-strengthened high entropy alloy: Scanning strategy dependent anisotropic mechanical properties

Wei Zhang [a], Hui Wang [b], Bart J. Kooi [b], Yutao Pei [a,*]

[a] Advanced Production Engineering, Engineering and Technology Institute Groningen, Faculty of Science and Engineering, University of Groningen, Nijenborgh 4, 9747 AG, the Netherlands

[b] Nanostructured Materials and Interfaces, Zernike Institute for Advanced Materials, Faculty of Science and Engineering, University of Groningen, Nijenborgh 4, 9747 AG, the Netherlands

ARTICLE INFO

Keywords:
Laser powder-bed fusion
High entropy alloy
Scanning strategy
Heterogeneous microstructure
Mechanical anisotropy

ABSTRACT

A non-equiatomic interstitial-strengthened high entropy alloy (iHEA), $Fe_{49.5}Mn_{30}Co_{10}Cr_{10}C_{0.5}$ (at.%), is manufactured by laser powder-bed fusion (LPBF) with stripe and chessboard scanning strategies. The present study highlights the correlation between the laser scanning strategies with resulting microstructure, textures, and anisotropic mechanical properties in as-built iHEA. The results show that the LPBF processed iHEA exhibits an excellent strength-ductility synergy due to the combined deformation mechanisms of dislocation slip, martensite phase transformation- and nano twinning-induced plasticity. The samples printed by the stripe scanning strategy show more evident mechanical anisotropy than that of the chessboard-scanned samples. The difference in the degree of mechanical anisotropy is mainly attributed to the heterogeneous grain morphology and crystallographic texture resulted from different scanning strategies.

1. Introduction

High entropy alloys (HEAs) have received extensive attention due to their high thermal stability, excellent mechanical properties and superior corrosion resistance, showing broad application prospects in the aerospace, automotive and energy industries [1–7]. In recent years, in order to overcome the strength-ductility trade-off problem in conventional single-phase HEAs, multiple non-equiatomic dual-phase HEAs systems have been successfully designed and fabricated based on the metastable engineering strategies [8,9]. In addition to the inherent solid solution strengthening, HEAs driven by novel strengthening and deformation mechanisms have also been reported, such as interstitial solid solution strengthening [10–13], precipitation strengthening [14–16], phase transformation- and/or twinning-induced plasticity (TRIP and TWIP, respectively) [17–22], providing new insights for the design of high strength-ductility material. Among these strategies, the introduction of small-sized interstitial atoms such as oxygen [10], carbon [11] and boron [12] to develop interstitial-strengthened HEAs (iHEAs) is promising for manipulating the superior mechanical properties. For example, a carbon-added non-equiatomic iHEA, $Fe_{49.5}Mn_{30}Co_{10}Cr_{10}C_{0.5}$ (at.%), can simultaneously activate the TRIP and TWIP deformation mechanisms, which enables this iHEA to have an improved strength-ductility synergy compared to the alloy without interstitial elements [11,18,20,23].

Over the past few years, additive manufacturing technology has developed rapidly, among which laser powder-bed fusion (LPBF), also known as selective laser melting (SLM), has become a favorable method for manufacturing HEAs components with complex geometry and superior mechanical properties due to its high-performance net-shape forming process characteristics [24–28]. Different from traditional casting technology, the molten pool in LPBF has the characteristics of large temperature gradient and fast cooling rate ($\sim 10^6$ K/s) [29], which can contribute to (i) the expansion of the solid solution limit, (ii) refined microstructure, and (iii) improved micro-segregation [30]. Moreover, the LPBF process has the effect of reciprocating reheating on the previous layers owing to the layer-by-layer deposition manner [31–35], which plays the role of in-situ heat treatment so that the as-printed materials can obtain microstructure different from traditional processing techniques.

Due to the large temperature gradient and the complex thermal history along the building direction, crystallographic textures and spatially heterogeneous distribution of grains often form in the LPBF manufactured parts, which usually lead to mechanical anisotropy [28, 36–39]. Some studies have shown that LPBF process parameters, such as

* Corresponding author.
E-mail address: y.pei@rug.nl (Y. Pei).

https://doi.org/10.1016/j.msea.2023.144978
Received 30 January 2023; Received in revised form 19 March 2023; Accepted 28 March 2023
Available online 31 March 2023

scanning speed [40], laser power [41] and scanning strategy [42–44], affect the relative density and microstructure of the as-printed samples, and eventually result in different mechanical properties. Among these parameters, the scanning strategy, which does not change the laser energy density but significantly affects the microstructure and mechanical anisotropy of the as-printed materials, has recently attracted the attention of scholars. Zhang et al. [42] studied the microstructure and mechanical properties of LPBF fabricated CoCrFeMnNi HEA with three different scanning strategies, namely '0-scan', '67-scan' and '90-scan' strategy, respectively. The results showed that the scanning strategy had a significant effect on the grain morphology, texture and residual stress distribution, thereby affecting the density and morphology of microcracks. The sample printed using the '67-scan' strategy had the lowest crack density and superior strength-ductility synergy. Guo et al. [44] studied the effect of scanning strategies on the mechanical properties and hot cracking behavior of LPBF manufactured CoCrFeMnNi-(N,Si) HEA. They found that the 45° scanning rotation strategy resulted in a higher hot crack density than the 67° rotation strategy, attributed to the pronounced epitaxial growth of columnar dendrites and the high local strain subjected in the alloy. In addition to the effects of the rotation angle, two standard scanning patterns in the LPBF process, namely stripe and chessboard, have also been reported to affect the mechanical properties of as-built metal materials [35,43]. Wang et al. [35] found that the GH4169 superalloy prepared by the chessboard pattern had higher tensile strength and more evident tensile anisotropy compared to the stripe samples, while opposite results were reported by Sun et al. [43] for the LPBF fabricated CoCrFeNi HEA using these two scanning patterns. Although some research work about the influence of scanning strategies on the mechanical response of LPBF printed HEAs has been carried out, the relationship between the heterogeneous microstructure and the corresponding mechanical anisotropy induced by different scanning strategies is still unclear and needs to be systematically studied. Therefore, it is necessary to determine the cause of the anisotropic mechanical properties according to the initial microstructure and texture characteristics, and analyze the difference in deformation behavior with respect to the loading direction.

In the present study, non-equiatomic $Fe_{49.5}Mn_{30}Co_{10}Cr_{10}C_{0.5}$ iHEA was fabricated by LPBF with stripe and chessboard scanning strategies. The grain morphology and crystallographic texture of the as-printed samples on different planes were comprehensively analyzed and discussed. The tensile mechanical properties were examined along three planes to study the mechanical anisotropy and its relationship with the heterogonous microstructure induced by different scanning strategies. The involved deformation mechanisms were discussed in detail based on multi-scale characterization methods.

2. Materials and methods

2.1. Sample fabrication

Gas-atomized non-equiatomic $Fe_{49.5}Mn_{30}Co_{10}Cr_{10}C_{0.5}$ (at.%) iHEA powder provided by Anhui Fitech Materials Company Ltd (China) was used as the raw material for LPBF. Fig. 1 shows the morphology of the powder, which has good sphericity with particle size in the range of 15–53 μm.

The LPBF process was carried out in SLM 125 HL system under an argon atmosphere. The process parameters including the scanning speed, laser power, hatch space and layer thickness were selected as 700 mm/s, 300 W, 120 μm and 30 μm, respectively. The volumetric energy density was calculated to be 119 J/mm^3. During the LPBF printing process, stripe and chessboard scanning patterns were applied with 33° rotation between consecutive layers, as schematically illustrated in Fig. 2a. The optimized 33° rotation angle was selected based on our screening experiments. For the chessboard scanning strategy, each layer was divided into multiple squares of 2 × 2 mm^2 size, and the scanning vectors in the adjacent squares were perpendicular to each other. The

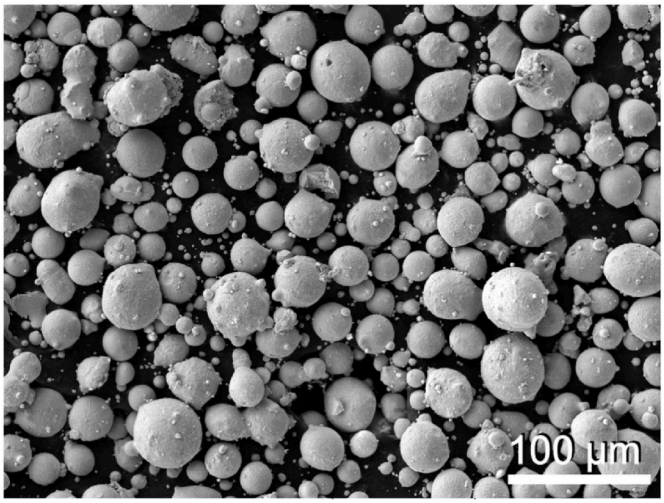

Fig. 1. SEM micrograph showing the morphology and particle size of gas-atomized $Fe_{49.5}Mn_{30}Co_{10}Cr_{10}C_{0.5}$ powder.

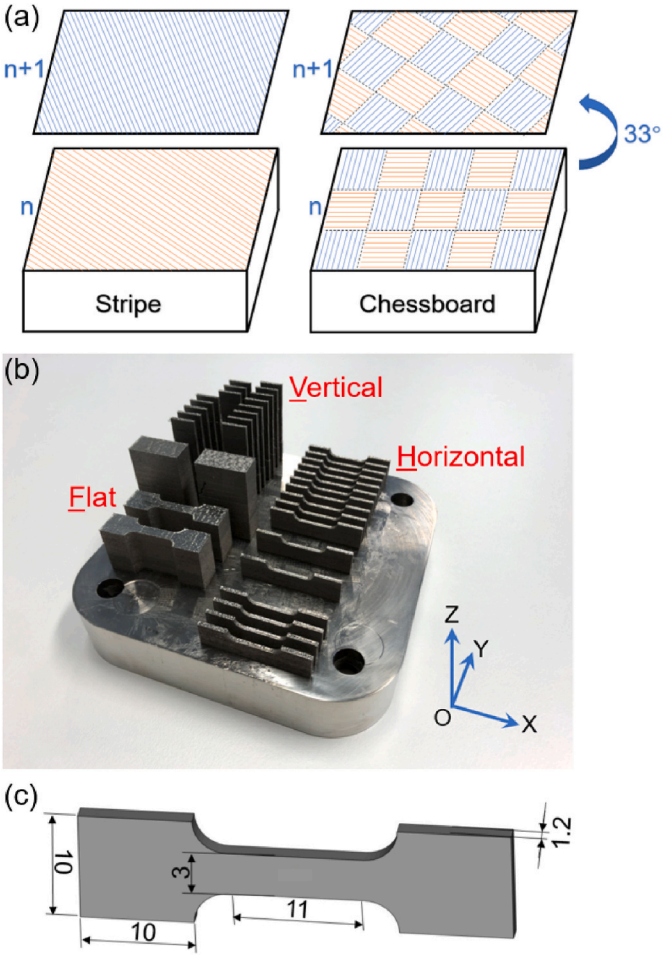

Fig. 2. (a) Schematic diagram of the stripe and chessboard scanning patterns; (b) LPBF printed iHEA samples orientated in three directions; (c) Dimensions of tensile samples in mm.

macroscopic image of the LPBF printed samples is presented in Fig. 2b, where the main direction of the laser beam scanning is described as X direction. To investigate the mechanical anisotropy of the LPBF fabricated samples, tensile samples were built in three directions for each

scanning pattern, and named as stripe-F (flat), stripe-H (horizontal), stripe-V (vertical), chessboard-F, chessboard-H and chessboard-V sample, respectively. The detailed dimensions of the tensile samples are shown in Fig. 2c.

2.2. Microstructure characterization and mechanical testing

To investigate the microstructure of LPBF built $Fe_{49.5}Mn_{30}Co_{10}Cr_{10}C_{0.5}$ iHEA, as-built samples with different printing planes were ground with #320-#4000 grit sand papers and then mechanically polished with 3 μm and 1 μm diamond suspension and finally OPS suspension. The microstructure and crystallographic orientation were analyzed by electron backscatter diffraction (EBSD) performed in a scanning electron microscope (SEM, Tescan Lyra) operated at 30 kV voltage. X-ray diffractometer (XRD, Bruker D8 Advance) was used to identify the phase constituents before and after tensile deformation. The XOY plane of the stripe-F sample was exposed to X-ray for XRD phase analysis.

The microhardness on the gauge plane of the as-printed tensile samples was measured by a Vickers microhardness tester with the applied load of 300 g and the dwelling time of 10 s, referring to the ASTM E384 standard. Twenty measurements were taken on each plane, and 0.5 mm distance between each indentation was maintained. To study the room-temperature tensile properties, tensile samples with gauge dimensions of 11 mm × 3 mm × 1.2 mm, which is a variety designed according to the sub-sized ASTM E8-E8M standard, were extracted by electrical discharge machining from the samples fabricated in different planes (Fig. 2b). Uniaxial tensile tests were performed using a Kammrath-Weiss tensile module at the strain rate of 3×10^{-4} s^{-1}. At least three tensile samples with respect to each loading direction were tested for the reproducibility of data. After the tensile test, both conventional EBSD and transmission EBSD analysis, as well as transmission electron microscopy (TEM) were performed near the fracture to investigate the deformation mechanisms of the additively manufactured iHEA. The transmission EBSD and TEM specimens were prepared with a focused ion beam (FIB), and the deformed microstructure was observed using a scanning transmission electron microscope (STEM) detector equipped in the SEM operated at 30 kV voltage. TEM analysis was performed using JEOL JEM-2200FS operated at 200 kV. The fracture morphology was observed with SEM to analyze the fracture behavior.

3. Results and discussion

3.1. Phase identification

The XRD patterns of the $Fe_{49.5}Mn_{30}Co_{10}Cr_{10}C_{0.5}$ iHEA powder, the as-printed sample on the XOY plane before and after tensile deformation (the stripe-F sample was used as representative) are shown in Fig. 3. Only the characteristic diffraction peaks of (111), (200), (220), (311) and (222) planes of the fcc crystal structure were detected in the as-received powder. In contrast, the hcp phase was observed in the as-printed and tensile tested samples. The reason for the formation of the hcp phase will be analyzed in detail in the microstructure section. Compared with the original powder, the relative peak intensity of (220) of the as-printed sample increased significantly. This implies that a preferential orientation of the grains was generated in the LPBF processed sample. It can also be observed that the peak intensities of the hcp phase increase relative to the ones of the fcc phase in the tensile deformed sample, indicating the formation of more hcp phase. This will be further scrutinized in the following section of mechanical property investigation.

3.2. Microstructures and crystallographic texture

Fig. 4 presents the 3D orientation maps of the LPBF built $Fe_{49.5}Mn_{30}Co_{10}Cr_{10}C_{0.5}$ iHEA samples using two scanning patterns. The

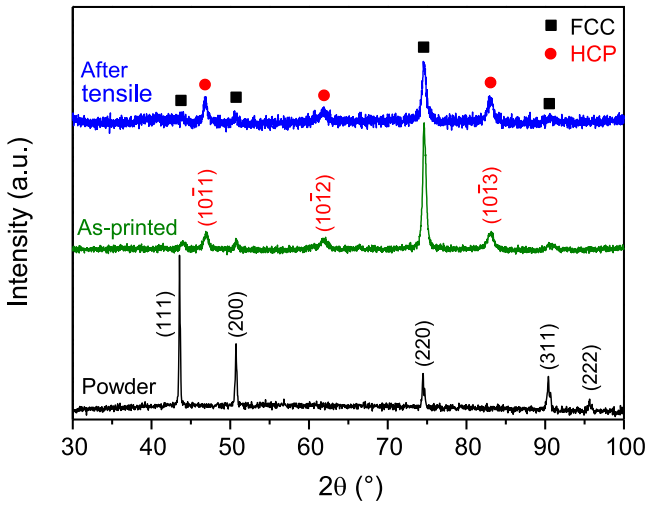

Fig. 3. XRD patterns of as-received powder, as-printed and tensile deformed iHEA samples.

unique morphology and texture of the LPBF fabricated iHEA are more obvious on the XOY plane of the stripe samples: the columnar grains are arrayed in a nearly rectangular shape with its shorter side along the laser scanning track (X direction) and longer side parallel to Y direction. For the chessboard samples, the laser beam passed discontinuously on the scanning plane, which led to the formation of interrupted linear arrangement of grains, as shown in Fig. 4d–f. Columnar grains and a few fine equiaxed grains can be observed in all samples. In particular, more equiaxed grains can be observed along the laser boundaries in the chessboard samples. Similar spatial heterostructures are often reported in LPBF built metallic materials [36,45–48], which usually show a visible periodicity corresponding to the applied laser scanning strategies [46].

A typical columnar grain structure can be observed along the building direction on the XOZ and YOZ planes of the flat and horizontal samples, which grows preferentially with length scales across several deposition layers, especially the stripe samples whose grain length is even larger than the whole EBSD scanning area (see Fig. 4a and b). For the vertical samples (Fig. 4c and f), the length of the columnar grains is reduced and the preferred orientation is significantly weakened. From these samples, it is noticed that the columnar grains can evolve heterogeneously with spatially different morphologies along the building direction. There are also some thin and fine grains near the grain boundaries of the coarse columnar grains (as indicated with blue arrows in Fig. 4). It is attributed to the complicated thermal gradient of the molten pool and its surrounding area in the LPBF process [46–48]. When the laser beam was scanned in parallel within each deposition layer, some fine grains preferentially grew along the centerline of the adjacent laser scanning paths, so the equiaxed shape could be observed on the XOY plane [46,47]. On the other hand, due to the large amount of heat input in the overlapping area between the successively scanned layers, larger columnar grains formed around the fine equiaxed grains [46]. Due to the 90° limitation window adopted by the present LPBF printer (exclude the entering rotation angles when the angle between the laser scanning direction and the airflow direction is less than 45°), the stripe samples show more inhomogeneous grain morphology and size on different planes of three differently orientated samples (Fig. 4a–c), while this microstructure heterogeneity of the chessboard samples is reduced to a certain extent due to the frequent change of the laser scanning direction among the small chessboard squares (Fig. 4d–f).

The average grain size and aspect ratio (based on the high angle grain boundaries) of different samples vary greatly, as listed in Table 1. For the flat and horizontal samples, although the XOY plane does have

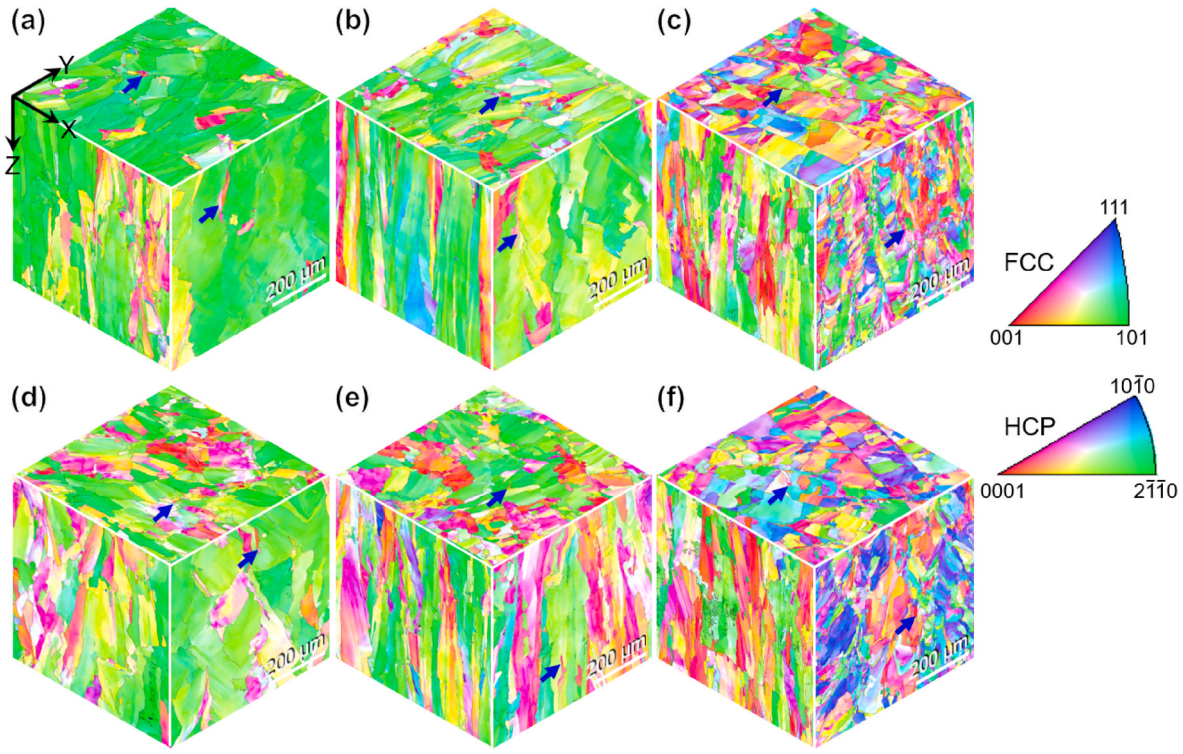

Fig. 4. EBSD orientation maps on the gauge planes of (a) stripe-F, (b) stripe-H, (c) stripe-V, (d) chessboard-F, (e) chessboard-H, and (f) chessboard-V samples. The color scheme of IPFs indicates the lattice orientations of fcc and hcp grains parallel to the Z direction (building direction of LPBF). The fine grains growing preferentially along the centerline of the adjacent laser scanning paths are indicated with blue arrows. (For interpretation of the references to color in this figure legend, the reader is referred to the Web version of this article.)

Table 1
Average grain size and aspect ratio in the XOY, XOZ and YOZ section planes of all samples.

Section plane	Average grain size (μm), aspect ratio					
	Stripe-F	Stripe-H	Stripe-V	Chessboard-F	Chessboard-H	Chessboard-V
XOY	91, 0.3	86, 0.4	57, 0.4	69, 0.4	63, 0.4	64, 0.4
XOZ	122, 0.2	229, 0.1	92, 0.2	120, 0.3	114, 0.4	76, 0.2
YOZ	343, 0.3	205, 0.3	38, 0.3	143, 0.3	115, 0.3	46, 0.3

some small grains distributed along the boundary of the molten pool, the proportion of coarse columnar grains is relatively high due to the temperature gradient and heat accumulation, so the average grain size on the XOZ and YOZ planes is large. The grain sizes of the chessboard-F and H samples are significantly reduced compared to the stripe-F and H samples, attributed to the formation of more equiaxed grains along the laser scan tracks in the former. While the aspect ratios of the chessboard-F and H samples are increased, and each sample exhibits less difference between the three section planes, indicating a relatively more uniform grain shape and size compared to the stripe samples. It is worth noting that for the vertical samples, both the scanning strategies led to a significant reduction in average grain size and a similar aspect ratio between different sections, which is related to the shape and size of the as-printed samples in the present study. Specifically, during the printing process of the gauge region of the vertical samples, the laser scanning area is small, approximately equal to the cross-sectional area (3×1.2 mm^2) of the tensile specimen, resulting in a decrease in the ratio of temperature gradient and solidification rate, that is, the degree of constitutional undercooling. Therefore, the growth of the columnar grains was inhibited, leading to the formation of finer grains and resultant similar aspect ratio. Furthermore, for the three different stripe samples, the difference in grain size between the XOZ and YOZ plane (221 μm, 24 μm and 54 μm for stripe-F, H and V, respectively) is significantly larger than that of the chessboard samples (23 μm, 1 μm and 30 μm for chessboard-F, H and V, respectively), which further indicates that the microstructure is less heterogeneous for the chessboard samples.

The corresponding EBSD phase maps for these six samples are provided in the Supplementary Material because of the small variability between the phase compositions. Both the stripe and chessboard samples have a large amount of fcc phase (more than 99%) with a very small amount of hcp phase distributed, as shown in Fig. S1. This is consistent with the XRD results in Fig. 3. LPBF is a complex heating and cooling process of multiple thermal cycles exposed to each deposited layer. Due to the difference in thermal conductivity between the substrate and the deposited layers, a large temperature gradient and cooling rate would be generated at the beginning of the printing process, where the fcc-hcp martensitic transformation could be kinetically suppressed. As the printing process progressed, the temperature gradient and cooling rate decreased with the gradually increased heat accumulation, promoting the formation of thermally induced martensitic transformation. In addition, due to the more complex laser scanning manner of the chessboard samples, it is speculated that the cooling rate is lower at the intersection of lasers in different directions, thus resulting in relatively more hcp phase in the chessboard samples.

Fig. 5 displays the (001), (110) and (111) pole figures and the inverse pole figure (IPF) taken from the XOY plane of stripe-F and chessboard-F samples. For these two samples, the columnar grains show a preferred

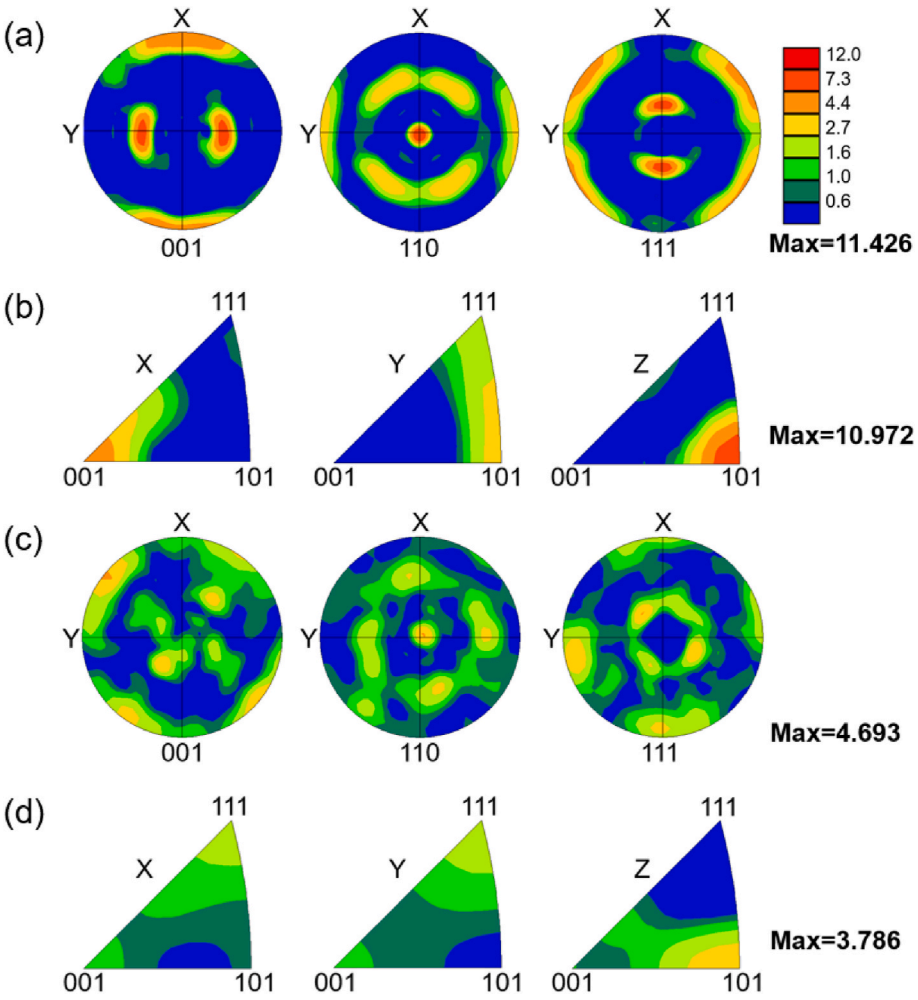

Fig. 5. EBSD pole figure and IPF texture taken from the XOY plane of as-built stripe-F sample (a, b) and chessboard-F sample (c, d).

<110> orientation parallel to the building direction, as indicated by the strong intensity peak observed at the center of the (110) pole figure, which is in good agreement with the strong (220) diffraction peak that appears on the XRD pattern of the as-printed sample (Fig. 3). There is also a strong <001> texture along the X direction of the stripe sample, as shown in Fig. 5a and b. Generally, it is known that the fcc crystal structure tends to grow in the preferred <001> orientation along the solidification direction during the additive manufacturing process [45,48,49]. However, when the scanning strategy between the two consecutive layers is rotated to a certain degree, the preferred orientation and intensity can be changed to some extent.

To be specific, during the LPBF process, when a laser beam travels along a certain direction, the molten pool is continuously solidified along the laser trajectory with the grains mainly growing along the <001> preferred orientation [36,45,48]. Due to the semi-elliptical shape of the molten pool, the latent heat is also radially transferred from the laser scanning center to the boundaries of the molten pool, causing the grains with <001> orientation to grow mostly along 0° and 45° with respect to the building direction [36]. This ensures the grains of the current scanning layer and the previously solidified grains maintain preferential growth in the direction with the largest temperature gradient [48,50]. However, due to the change of the laser scanning angle for every two consecutive layers in this study, the growth of crystal grains along 0° from the bottom of the molten pool would be suppressed to a certain extent. Therefore, most of the solidified crystals from the molten pool boundaries would grow at 45° from the building direction, indicating that not only the <001> texture was generated in the X direction, but also the strong <110> texture was generated in the Y and Z directions [48,50]. The above-mentioned preferred orientation of grain growth is more obvious in the stripe samples, as shown in Fig. 5a and b. For the chessboard samples, due to the frequent changes of the laser scanning direction in small square areas between two consecutive deposition layers, the continuous growth of the grains along both 0° and 45° was suppressed. As a result, the texture intensity of the grains was significantly reduced compared to the stripe sample, with the maximum value dropped from 11.426 to 4.693. Some <111> orientated grains along the X and Y directions were also observed in the chessboard sample as shown in Fig. 5d, which was also found in GH4169 superalloy printed by LPBF using the chessboard scanning strategy [35], demonstrating that a relatively more random crystallographic orientation can be obtained by adjusting the scanning pattern in LPBF additive manufacturing process.

3.3. Mechanical anisotropy and strengthening mechanisms

3.3.1. Microhardness

The microhardness on the gauge planes of different samples is presented in Fig. 6, which is obtained from 20 measuring points on each sample. The average microhardness values of the stripe-F, H and V samples are 287.9 $HV_{0.3}$, 287.6 $HV_{0.3}$ and 255.3 $HV_{0.3}$, respectively. The corresponding values for the chessboard samples are 284.7 $HV_{0.3}$, 279.9 $HV_{0.3}$, and 283.4 $HV_{0.3}$, respectively. It is worth noting that the measured values and the grain sizes on each plane mentioned above do not satisfy the Hall-Petch relation, which is related to the difference in

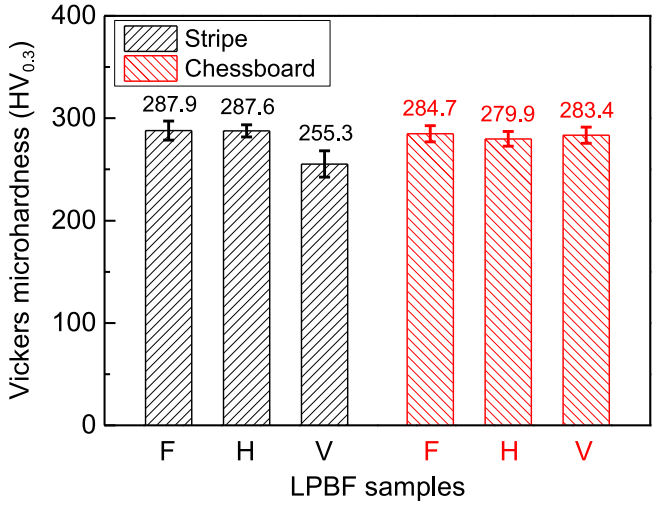

Fig. 6. Vickers microhardness distributions of different samples.

sub-grain size and initial dislocation density, because these factors also significantly affect the Hall-Petch relationship [51,52]. Moreover, it can be noticed that the microhardness distribution on different planes of the chessboard samples is more uniform than the stripe samples, mainly due to the more homogeneous microstructure in the chessboard samples.

3.3.2. Tensile properties and deformation mechanisms

The tensile engineering stress-strain curves of the LPBF printed stripe and chessboard samples along different directions are shown in Fig. 7a. It can be observed that the stress-strain curves of the stripe samples change within a certain range. The stripe-H sample exhibits the highest ultimate tensile strength (UTS) of 1102 MPa and elongation of 47%, and the stripe-F sample shows the lowest UTS of 980 MPa and an elongation of 37% at fracture. This difference in mechanical properties is significantly reduced between the chessboard samples. In other words, it is confirmed that the additively manufactured $Fe_{49.5}Mn_{30}Co_{10}Cr_{10}C_{0.5}$ iHEA shows mechanical anisotropy, and the degree of anisotropy is related to the applied scanning strategy during the LPBF process, which has also been reported in Ref. [35].

Fig. 7b shows a comparison of the yield strength (YS), UTS and uniform elongation of the printed stripe and chessboard samples along different loading planes. The variations of the YS in different planes of both the stripe and the chessboard samples are consistent with the observed changes of the microhardness. For the stripe samples, the UTS and uniform elongation of different samples exhibit more significant anisotropy compared to the YS, which is mainly associated with the crystal orientation and deformation characteristics along these loading planes. The degree of plastic deformation and mechanical strength of the metallic material mainly depends on the dislocation slip governed by the crystal orientation and the loading direction. Only when the stress acting on the slip plane along the slip direction reaches the critical resolved shear stress will slip proceed [51]. For an fcc alloy, the difficulty of slip is ordered accordingly as [111] > [110] > [001] [49,51]. In the LPBF printed stripe samples, the columnar grains mainly grow along the building direction with a preferred <110> orientation (as shown in Figs. 4 and 5). When the external force acts in the X direction (the situation of flat and horizontal tensile samples), on one hand, as the loading direction is parallel to the <001> orientation of the columnar grains, it is conducive to the occurrence of slip and promotes the steady and continuous plastic deformation, thereby increasing the elongation of the material. On the other hand, as the angle between the columnar grains and the loading force is approximately 90°, the columnar grains are more prone to cracking [51]. However, it can be seen from Fig. 7a and b that there is a significant difference in the tensile properties

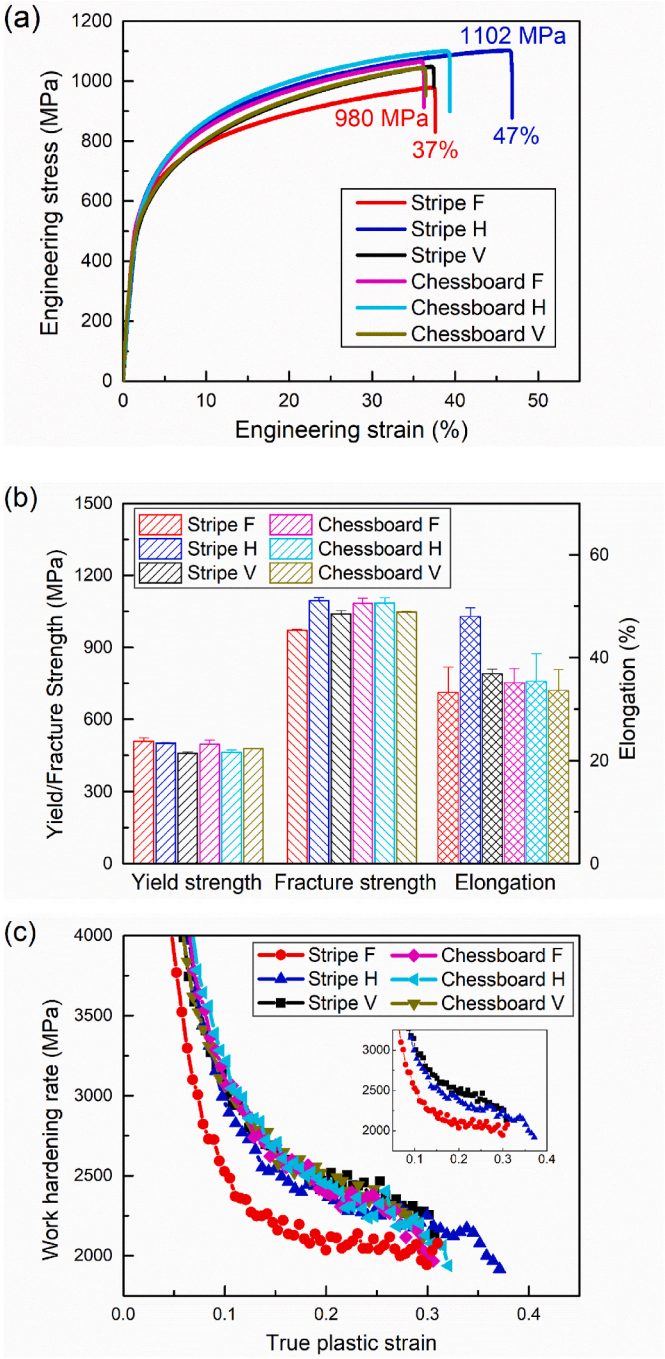

Fig. 7. (a) Tensile engineering stress-strain curves; (b) Comparison of the yield strength, fracture strength and elongation between stripe and chessboard samples; (c) Work hardening rate curves.

between the stripe-F and H samples. This is because the stripe-F sample has more grain boundaries and more pore defects due to the track-by-track laser-scanning pattern, and it is easier for cracks to propagate along the grain boundaries during the loading process, leading to the reduced strength and elongation, which will be confirmed by the fracture topography analysis discussed below.

When the tensile load is applied in the building direction (the situation of the vertical tensile samples), the loading direction is parallel to the <110> orientation of the grains, where the slip of the crystal grains is hindered to a certain extent, so the degree of plastic deformation is reduced. Meanwhile, owing to the layer-by-layer printing method of LPBF, there are more micro-pores in the vertical sample (revealed by the

fracture topography in Fig. 12c and f), which causes the micro-cracks to easily generate at the grain boundaries during the loading process, and ultimately reduce the fracture strength and elongation. In comparison, the chessboard samples exhibit decreased elongation, mainly related to the increased porosity and residual stress [35], but the difference in YS, UTS and elongation along different loading planes is significantly reduced due to the more homogeneous microstructure. It needs to be mentioned that despite the extremely larger grain size and lower amount of hcp phase, the mechanical strength of the present iHEA is higher than that of the cast and heat-treated samples with a grain size of 4–40 μm [11,18,20], while the total elongation is slightly decreased. This is related to the formation of $M_{23}C_6$ and M_7C_3 precipitates in the microstructure, which has been confirmed by the high energy synchrotron XRD analysis in our previous study [53]. The formation of nano-carbide precipitates is associated with the addition of carbon interstitials in the microstructure, which can effectively hinder the dislocation movement and generate high back stress-induced hardening through massive geometrically necessary dislocations (GNDs) during plastic deformation, further contributing to the strengthening of this alloy [54,55]. These carbide precipitates have been reported to block dislocation movement more effectively than sub-grain boundaries [55], suggesting that the volume fraction of carbides can be a crucial factor for modulating the mechanical properties of HEAs containing carbon interstitials. In addition to the precipitation strengthening effect, the current iHEA also benefits from interstitial solid solution strengthening. This is due to the fact that carbon interstitials cause much higher lattice distortions than substitutional elements, which strongly affects their interactions with dislocations [11].

Fig. 7c shows the relationship between the work hardening rate (WHR) and the true strain of the stripe and chessboard tensile samples loaded along different planes. The inset in Fig. 7c illustrates a pronounced anisotropy of the work hardening ability of the stripe samples. The initial WHR of the stripe-F sample is much lower than that of the stripe-H and stripe-V samples, which tendency leads to the relatively poor mechanical properties of the stripe-F sample. The WHR curves of the chessboard samples are much more similar in different loading planes. The above results indicate that the plastic deformation and work hardening mechanisms of the stripe samples exhibit obvious anisotropy, while the anisotropy of the chessboard samples is significantly weakened.

Stable work hardening ability under high stress levels is mainly attributed to the activation of multiple deformation mechanisms, which is essential for the material to maintain a large uniform elongation during the loading process [24]. In general, the work hardening of a material is caused by the accumulation of a large number of dislocations during deformation, where the mean free path of dislocation movement will decrease as the total dislocation density increases [36,56,57]. The activation and interaction of multiple slip systems during plastic deformation process can further promote the work hardening behavior of the material. More importantly, the formation of deformation-induced hcp martensite phase in the present study (which will be discussed in detail later) not only carries the plastic deformation, but also provides a strong barrier for the movement of dislocations, both of which can significantly enhance the work hardening ability [18,19]. Therefore, the deformation mechanisms mainly including dislocation-mediated plasticity and TRIP effect essentially maintain the stable work hardening behavior of the present LPBF printed iHEA, leading to superior mechanical properties.

As observed in some recent studies [36,39,50,58–61], the spatially heterogeneous grain structures and crystallographic textures directly affect the deformation incompatibility and anisotropic hardening behavior of LPBF fabricated materials. Im et al. [59] pointed out that in the 316L stainless steel, due to the accumulation of more GNDs, the loading direction across the short axis of the columnar grains was conducive to getting more work hardening than loading along the long axis of the columnar grains. This is consistent with the horizontal tensile samples in the present study. These GNDs caused by the heterogeneous grain structure can introduce a long-range internal stress opposite to the loading direction, which not only contributes to the Hall-Petch relationship, but also improves the work hardening ability of the material through impeding the dislocation movement [36,52].

The Taylor model describes polycrystalline deformation based on the slip of individual crystals, which has been widely used to explain and predict strength, ductility and texture evolution during deformation [35,62,63]. The Taylor factor (TF) is an average orientation factor that describes the propensity of a crystal to slip (or not) based on its orientation relative to the macroscopic stress state, depending on the texture of the material and the crystallographic nature of the assumed slip systems. The TF represents the ability of a material to resist plastic deformation, and grains with large TF values indicate that a large amount of slip is required to consume plastic work during deformation [35]. Higher dislocation density is generated inside these grains to maintain the strain compatibility with neighboring grains, resulting in lower effective stacking fault energy (SFE) [64]. Therefore, high flow stresses are expected to develop in these grains. To compare the deformation resistance of the stripe and chessboard samples along different tensile planes, TF maps were constructed based on the uniaxial tensile direction relative to the {111}<110> slip system within each grain. Fig. 8 shows the TF distribution maps on the gauge planes of different samples. Also, the average TF, considering all the detected grains in the EBSD map of the samples, is listed at the top of each panel in Fig. 8.

Comparing the samples loaded along different planes, the average TF of the stripe-H and V samples is 2.58 and 3.06, respectively, which are quite close to those of the chessboard-H and V samples, indicating that the stripe and chessboard samples have similar resistance to plastic deformation in these two loading planes. In contrast, the stripe-F sample exhibited a clearly lower TF (2.68) than that of the chessboard-F sample (3.17), consistent with the tensile test results (Fig. 7). The grains in the stripe-F, stripe-H and chessboard-H samples show lower TF values compared to other samples. This signifies that the <001> fiber texture (TF = ~2.45 [57,65]) strongly contributed to the flow stress in these samples, while <110> texture (TF = ~3.67 [61]) and <111> texture (TF = ~3.67 [57,65]) also contributed to other samples, which is consistent with the texture analysis results shown in Fig. 5. Therefore, for the present iHEA samples processed by LPBF under different scanning strategies, the difference in deformation behavior and mechanical anisotropy can be explained by the different TFs caused by the texture in different planes concerning each loading direction.

As analyzed with XRD shown in Fig. 3, both fcc and hcp phases were detected in the sample before and after tensile tests. The relative intensity of the characteristic diffraction peaks of the fcc and hcp phases changed after tensile test, indicating that a phase transformation from fcc to hcp occurred during the plastic deformation. The EBSD mapping given in Fig. 9a–d shows the microstructure of the stripe-V sample after tensile test, and the chart in Fig. 9e depicts the misorientation angle between the fcc and hcp phases. Lath-like hcp phase can be observed inside the fcc matrix through the deformation induced phase transformation, where the thin hcp laths showed a tendency to gradually thicken and grow towards each other, thereby promoting the formation of a massive amount of hcp phase, i.e. a volume fraction of 29.1% at fracture. The detailed orientation relationship of fcc and hcp phases can be found in Fig. 9f, where a standard Shoji-Nishiyama orientation relationship ($<110>_{fcc}//<11\text{–}20>_{hcp}$) was confirmed by the corresponding pole figure of fcc and hcp phase in the deformed sample. The misorientation angle between these two phases is about 45.8°. From Fig. 9, a large number of slip bands were also found with a misorientation angle of 2.5° within the fcc phase. These slip bands were generated by the slip of Shockley partial dislocations and acted as the cores for the martensite nucleation. Therefore, it is believed that massive slip bands should have been generated in the fcc phase during the deformation process to realize the martensite transformation [56].

The SFE plays an extremely critical role in affecting the plastic

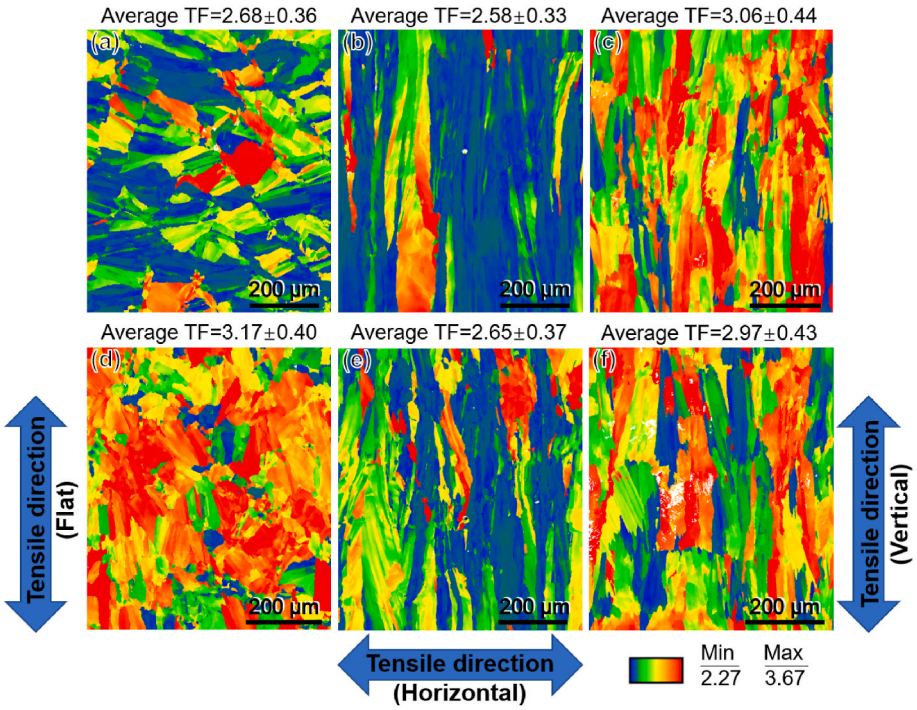

Fig. 8. Taylor factor maps of the as-built $Fe_{49.5}Mn_{30}Co_{10}Cr_{10}C_{0.5}$ iHEA with respect to different tensile directions on (a) stripe-F, (b) stripe-H, (c) stripe-V samples, and (d) chessboard-F, (e) chessboard-H, (f) chessboard-V samples.

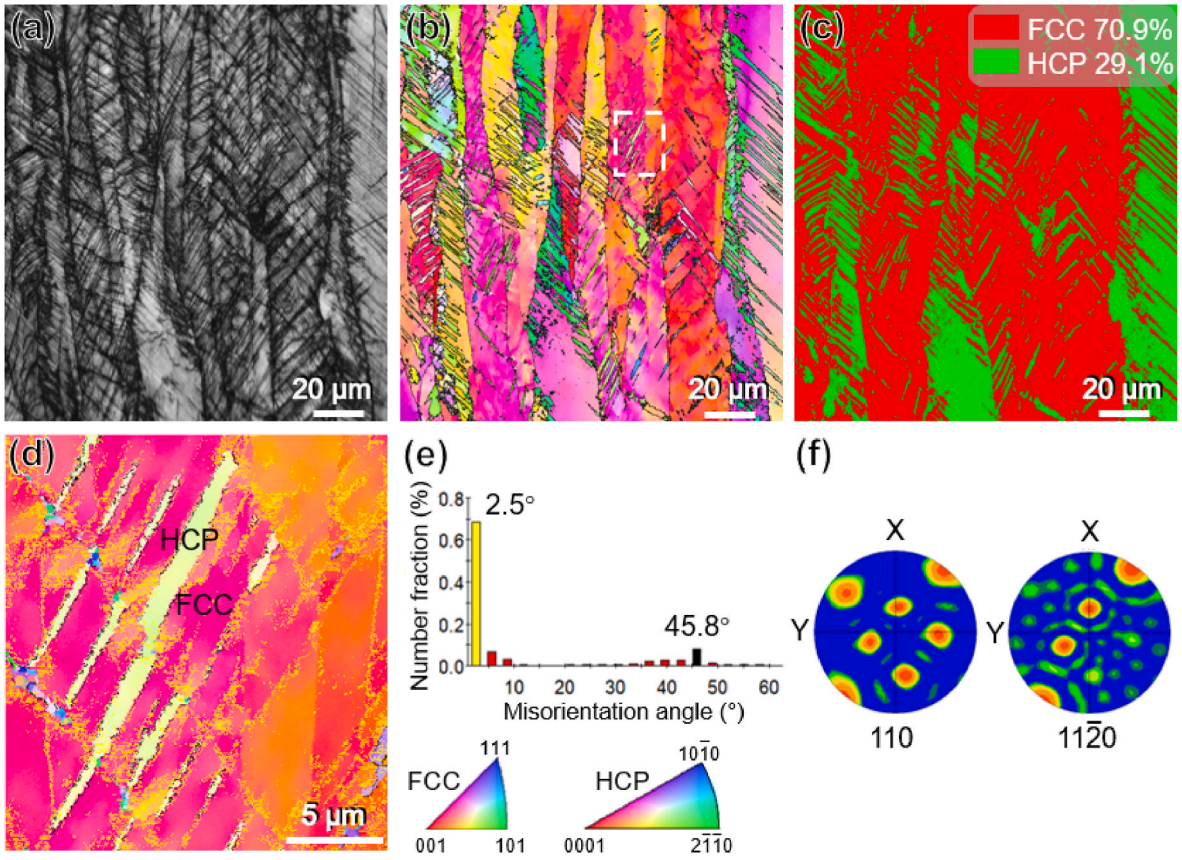

Fig. 9. (a) Banding structure revealed in EBSD image quality map, (b) IPF map and (c) phase map showing the deformed microstructure; (d) Magnified IPF map of a local area marked in (b); (e) Misorientation angle distribution in (d); (f) Pole figure of the fcc and hcp phase in (d).

deformation behavior of fcc phases [66,67]. With the gradual decrease of SFE, the plastic deformation mode changes from dislocation-mediated slip to deformation twins, and finally to fcc-hcp phase transformation [68]. In fcc alloys with low SFE, a unit dislocation with 1/2<110> Burgers vector tends to dissociate into two Shockley partial dislocations with 1/6 <211> Burgers vector according to Frank's rule. Either deformation twining or fcc-hcp martensitic transformation is proceeded by the movement of Shockley partial dislocations. If the Shockley dislocations slide on every two consecutive $\{111\}_{fcc}$ close packed planes, deformation twins will be produced, while the fcc-hcp phase transformation will be generated if the Shockley dislocations slide on every second $\{111\}_{fcc}$ close packed plane [68,69]. It has been reported that the SFE of CoCrFeMnNi HEA is significantly affected by the SFE of each constituent element [19,70,71]. The value of intrinsic SFE of the equiatomic CoCrFeMnNi HEA is 20–50 mJ/m^2 [72,73]. The effect of carbon interstitials on SFE varies in different HEA systems [23,74]. For the present non-equiatomic $Fe_{49.5}Mn_{30}Co_{10}Cr_{10}C_{0.5}$ iHEA, carbon interstitials slightly increase the SFE to a critical point of around 18 mJ/m^2 [23]. This facilitates the fcc-hcp phase transformation and makes it the dominant plastic deformation mechanism in the metastable fcc phase at room temperature [68,75–79]. During the deformation process, the fcc-hcp phase transformation plays an increasingly important role in

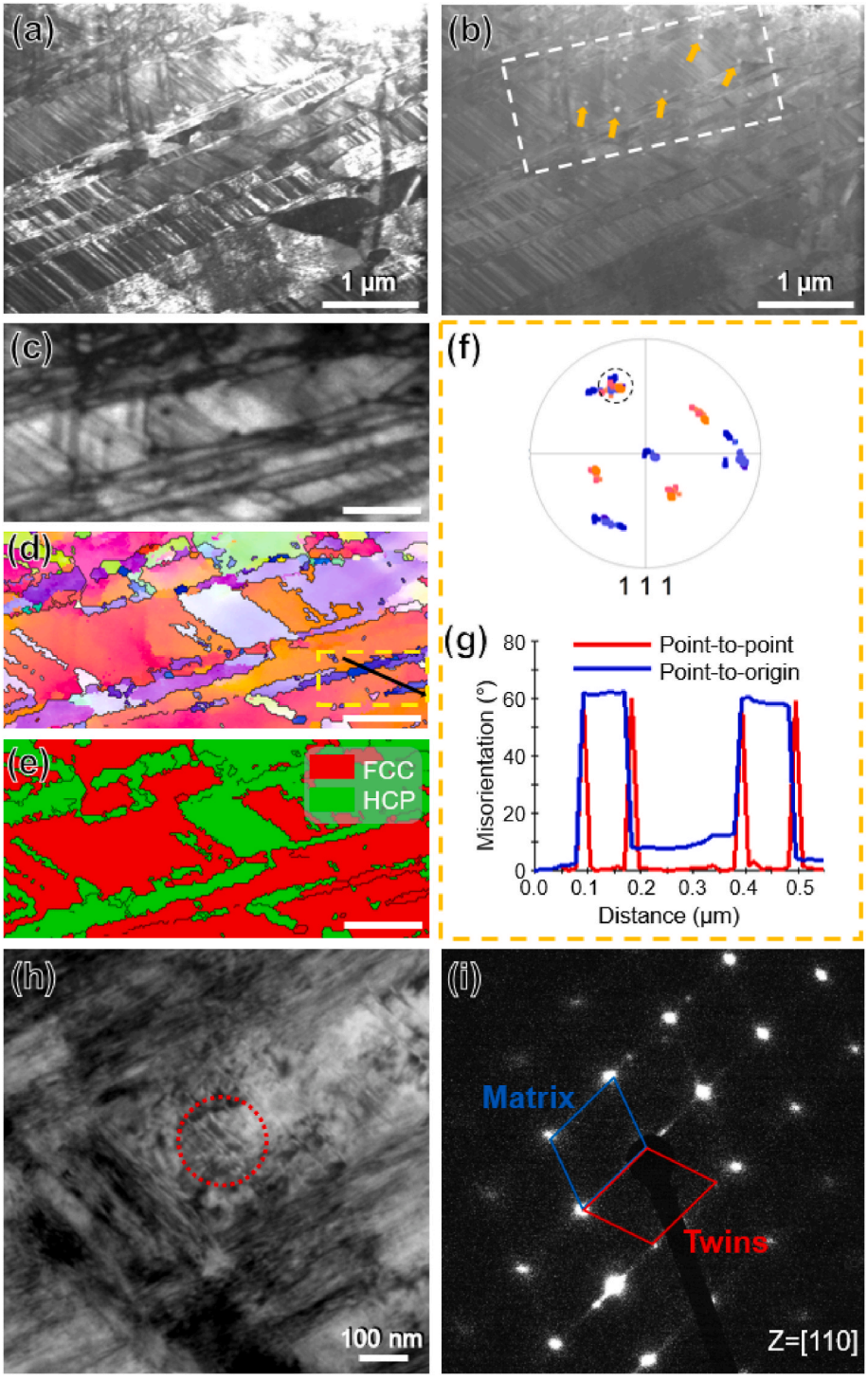

Fig. 10. (a) Bright-field STEM image with (b) the dark-field image showing the deformation microstructure near the fracture; (c–e) Transmission EBSD results from the area marked in (b), the scale bar is 500 nm; (f) Pole figure for the fcc matrix and twin obtained from the area marked in (d); (g) Misorientation profile along the black line in (d); (h) Bright-field TEM image of the fractured sample with the corresponding SAED pattern in (i) showing deformation twins from the selected area (in red circle). (For interpretation of the references to color in this figure legend, the reader is referred to the Web version of this article.)

accommodating the plasticity to maintain the stable work hardening ability under high stress levels and superior strength, as the martensitic hcp phase also plays a role in secondary hardening due to the lack of plasticity in the hcp structure [24,68,75–79]. As a result, this LPBF processed iHEA exhibited an excellent strength-ductility combination.

In addition, it can be observed from Fig. 9 that the fcc-hcp phase transformation mainly occurred in grains with specific orientations, such as the grains with <110> axis parallel to the tensile direction. Due to the difficulty of slip, multiple slip systems were activated for the basal slip in these grains to cause dislocations pileup, which led to the reduction of effective SFE and thus promoted the phase transformation [80]. In contrast, the deformation mechanism of the <001> oriented grains is mainly dislocation slip, as this orientation is conducive to continuous and stable dislocation slip. Therefore, the crystallographic orientation of fcc grains plays an important role in the directional flow behavior by adjusting the activity of TRIP.

Fig. 10 shows the STEM, transmission EBSD and TEM images of the stripe-V sample near the fracture area after tensile test, revealing more deformation behaviors at nanoscale level. From the bright-field STEM image (Fig. 10a), distinct deformed lath-like structures can be observed. In the dark-field image, nanoscale circular precipitates are observed, as indicated by the yellow arrows in Fig. 10b, verifying the precipitation strengthening mechanism mentioned before. The transmission EBSD observation position is marked with the white dashed line in Fig. 10b. From Fig. 10c–e, it can be observed that in addition to the deformation-induced fcc-hcp phase transformation, there is also an fcc single-phase structure with obvious misorientation in the matrix, as marked by a yellow dashed rectangle in Fig. 10d. According to the presence of a coincident point in the {111} pole figure (marked with a black dashed circle in Fig. 10f, which indicates that the matrix and the lath-like structure have a mirror-symmetric relationship with the {111} plane) and the sharp peaks with misorientation angle of 60° along the black line in Fig. 10d, it can be concluded that in addition to the significant fcc-hcp transformation, there is also a small amount of deformation-induced twinning formation. The thickness of these twins was measured as around 50 nm in the high magnification EBSD image. The bright-field TEM micrograph near fracture shown in Fig. 10h and the corresponding SAED analysis (Fig. 10i) performed in the red circle area further confirm the existence of nanoscale deformation twins in the fcc matrix. Despite the low content of deformation twinning, the similarity in morphology between the deformation-induced hcp phase and the nano-sized twins, and the continuity of the interface between them imply that the fcc-hcp transformation and twinning developed simultaneously, jointly facilitating the superior mechanical properties of the additively manufactured iHEA.

To further reveal the deformation characteristics of different orientated samples, the surfaces near the fracture region after tensile test were observed by SEM, and the results are presented in Fig. 11. The stripe-F sample, as shown in Fig. 11a, which has a relatively lower WHR during the deformation process, severely deformed in a specific direction within each grain, with the traces of slip bands on the surface approximately perpendicular to the loading direction. In contrast, the fracture surface of the stripe-H sample presents a 45° shear shape (Fig. 11b), and the slip bands are approximately parallel to the loading direction, where the secondary slip bands can also be observed, suggesting more pronounced ductility. The stripe-V sample with higher WHR, shows obvious cross slip bands on the deformed surface (Fig. 11c). The deformation proceeded in a more homogeneous mode in this stripe-V sample is thought to be the result of the grains showing weaker preferred orientation along the loading direction (Fig. 4c), where

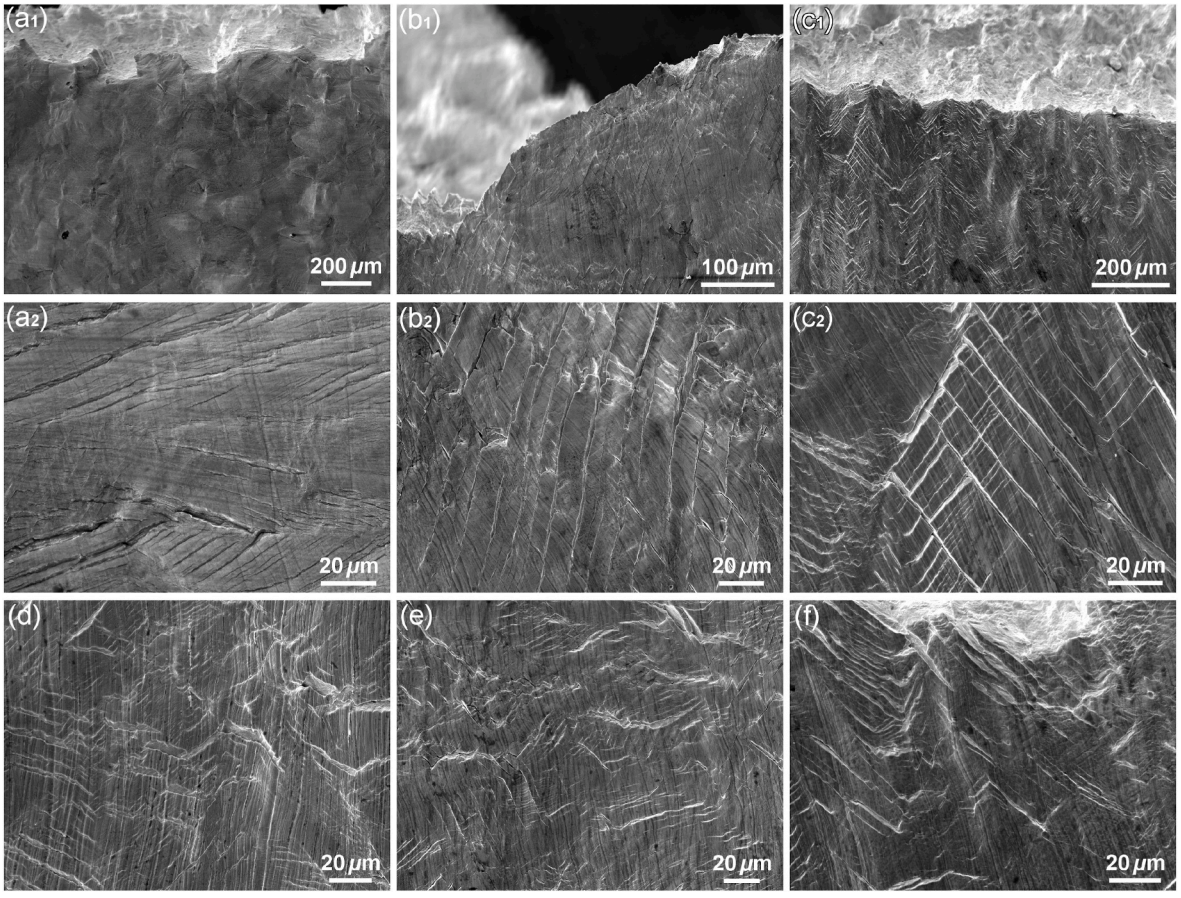

Fig. 11. Deformation characteristics of different tensile samples: (a) stripe-F, (b) stripe-H and (c) stripe-V samples; (d) chessboard-F, (e) chessboard-H and (f) chessboard-V samples.

multiple slip systems were activated for the basal slip due to the difficulty of slip in these grains. The difference in the slip direction of the slip bands further confirms the mechanical anisotropy in the above three samples. For the chessboard samples, the heterogeneity of the fracture surface morphology has been significantly improved. As shown in Fig. 11d–f, the crossed slip bands can be observed on the surface of all tensile samples, which benefits from the less heterogeneous grain orientation (Figs. 4 and 5). Based on the above analysis, it can be concluded that the use of chessboard scanning strategy can improve the homogeneity and mechanical anisotropy of the LPBF processed materials.

The fracture morphology of the tensile tested samples was analyzed to further study the fracture mechanism. Fig. 12a–c shows the fracture surfaces of the stripe-F, H and V samples, respectively. Some spherical gas-driven pores and microcracks can be clearly observed on all fracture surfaces. The gas-driven pores are characterized by smooth inner surfaces, small size and round shape, usually originating from the gas entrapped inside the powder materials or the molten pool [81], which are different from the irregularly shaped lack-of-fusion (LoF) pores. The latter usually forms as a result of incomplete powder melting. There are also a large number of dimples on these fracture surfaces, revealing a dominant ductile fracture behavior. Nevertheless, the tensile-fractured stripe samples along different planes still exhibited various fracture characteristics. For the stripe-F sample, although ductile dimples are observed on the fracture surface, some small cleavage fracture surfaces parallel to the Y direction (along the horizontal direction in Fig. 12a) are also detected, corresponding to the above-mentioned slip bands that are approximately perpendicular to the tensile direction. While fine dimples are mostly distributed on the fracture surface of the stripe-H sample, indicating that it has experienced severe plastic deformation corresponding to the largest elongation. The fracture surface of the stripe-V sample shows more gas pores and microcracks, which is related to the layer-by-layer and track-by-track printing mode of LPBF. It introduced more molten pool boundaries in the vertical direction, where microscopic defects tend to generate during the LPBF process [82,83].

Fig. 12d–f presents the fracture surfaces of the chessboard-F, H and V samples, respectively. Compared with the stripe samples, more gas pores, LoF pores and microcracks can be observed on the fracture surfaces of the chessboard samples. This implies that the chessboard samples are more prone to cracking, as cracks usually initiate near the LoF pores which often form at the borders of the square domains of chessboard. However, due to the frequent change of the grain orientation and the increase of high-angle grain boundaries, the propagation of cracks during the tensile process would also be hindered, resulting in no obvious deterioration in the mechanical properties of the chessboard samples compared to the stripe ones. It can also be seen that the difference in fracture morphology of these three differently orientated samples is reduced compared with the stripe samples, which is consistent with the similar cross-slip bands in Fig. 11d–f.

4. Conclusions

In this study, the microstructures, anisotropy of tensile properties and deformation mechanisms of $Fe_{49.5}Mn_{30}Co_{10}Cr_{10}C_{0.5}$ iHEA printed by LPBF under stripe and chessboard scanning strategies were investigated systematically. The main conclusions drawn are as follows.

(1) An fcc matrix decorated with a negligible amount of hcp phase was generated in the LPBF processed non-equiatomic $Fe_{49.5}Mn_{30}Co_{10}Cr_{10}C_{0.5}$ iHEA. Both the stripe and chessboard

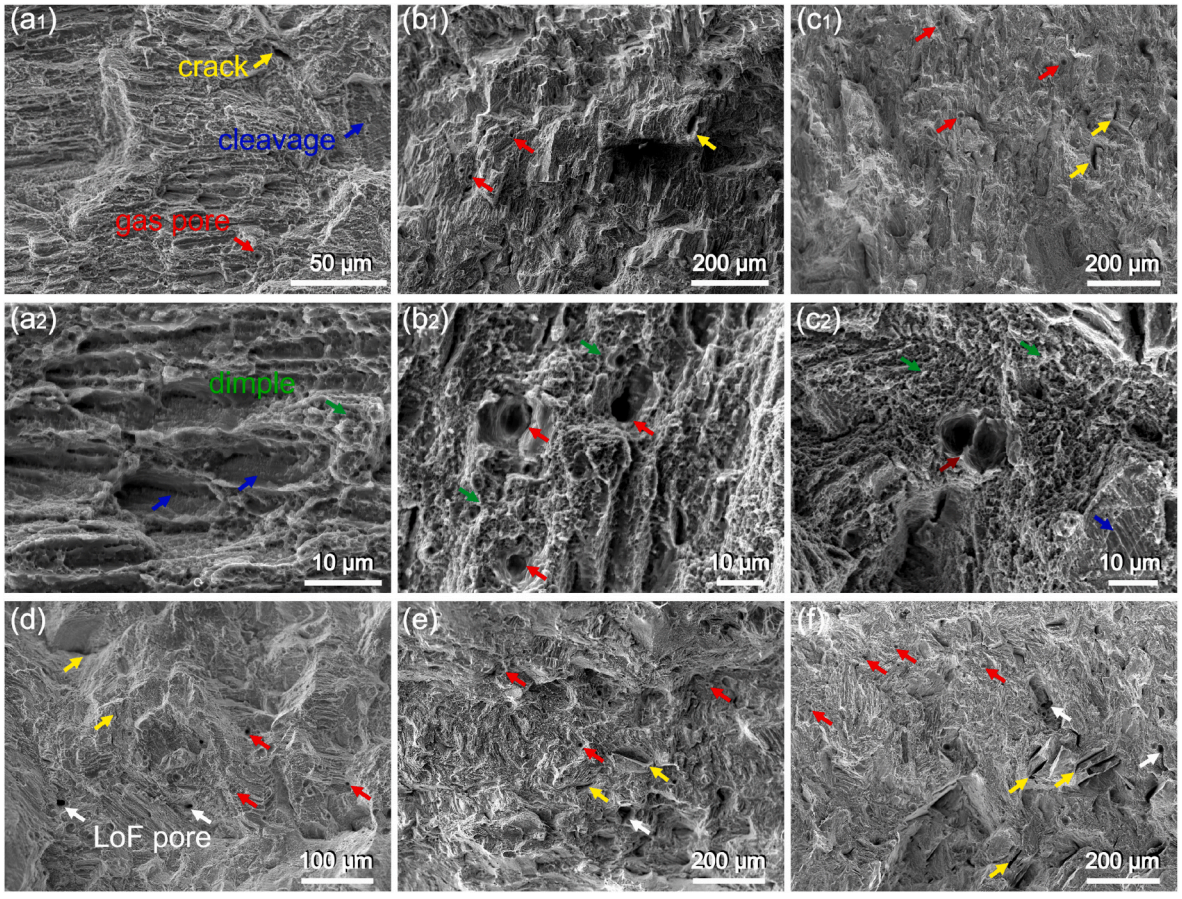

Fig. 12. Fracture morphology of tensile tested samples: (a) stripe-F, (b) stripe-H and (c) stripe-V samples; (d) chessboard-F, (e) chessboard-H and (f) chessboard-V samples.

samples are composed of columnar and equiaxial grains with a preferred <110> orientation parallel to the building direction, while a strong <001> texture parallel to the laser scanning direction was also formed in the stripe samples, arising from the interaction between the preferential growth mechanism of the grains and the direction of the temperature gradient during the LPBF process.

(2) The microhardness, yielding strength, ultimate tensile strength and fracture elongation of the stripe samples loaded along three different planes showed more evident mechanical anisotropy compared to the chessboard samples, mainly attributed to the grain structure and crystallographic texture generated by different laser scanning strategies.

(3) Carbon interstitials in the current $Fe_{49.5}Mn_{30}Co_{10}Cr_{10}C_{0.5}$ iHEA contributed to both the precipitation strengthening and interstitial solid solution strengthening. Plastic deformation process is accommodated by dislocation slip, phase transformation and nano-twinning, contributing to the excellent combination of strength and plasticity of the LPBF processed iHEA. The crystallographic texture plays an important role in the deformation mechanisms by governing the deformation activity.

(4) All samples showed ductile fracture with the formation of a large number of dimples. Some small cleavage surfaces in the stripe samples and lack-of-fusion pores in the chessboard samples could also be observed from the fracture. The deformation characteristics and fracture morphology under different scanning patterns also showed inhomogeneity.

CRediT authorship contribution statement

Wei Zhang: Funding acquisition, Conceptualization, Methodology, Investigation, Data curation, Formal analysis, Visualization, Validation, Writing – original draft. **Hui Wang:** Data curation, Formal analysis, Writing – review & editing. **Bart J. Kooi:** Supervision, Writing – review & editing. **Yutao Pei:** Funding acquisition, Conceptualization, Methodology, Supervision, Writing – review & editing.

Declaration of competing interest

The authors declare that they have no known competing financial interests or personal relationships that could have appeared to influence the work reported in this paper.

Data availability

Data will be made available on request.

Acknowledgment

W.Z. acknowledges the China Scholarship Council for funding her Ph.D. grant (CSC NO. 201906250212). Samenwerkingsverband Noord-Nederland (SNN) is thanked for financial support within the program “3D Print Kompas”.

Appendix A. Supplementary data

Supplementary data to this article can be found online at https://doi.org/10.1016/j.msea.2023.144978.

References

[1] Y. Zhang, T.T. Zuo, Z. Tang, M.C. Gao, K.A. Dahmen, P.K. Liaw, Z.P. Lu, Microstructures and properties of high-entropy alloys, Prog. Mater. Sci. 61 (2014) 1–93.
[2] Z. Li, F. Kormann, B. Grabowski, J. Neugebauer, D. Raabe, Ab initio assisted design of quinary dual-phase high-entropy alloys with transformation-induced plasticity, Acta Mater. 136 (2017) 262–270.
[3] C.P. Lee, C.C. Chang, Y.Y. Chen, J.W. Yeh, H.C. Shih, Effect of the aluminium content of $Al_xCrFe_{1.5}MnNi_{0.5}$ high-entropy alloys on the corrosion behaviour in aqueous environments, Corrosion Sci. 50 (2008) 2053–2060.
[4] C.L. Tracy, S. Park, D.R. Rittman, S.J. Zinkle, H. Bei, M. Lang, R.C. Ewing, W. L. Mao, High pressure synthesis of a hexagonal close-packed phase of the highentropy alloy CrMnFeCoNi, Nat. Commun. 8 (2017), 15634.
[5] D.B. Miracle, O.N. Senkov, A critical review of high entropy alloys and related concepts, Acta Mater. 122 (2017) 448–511.
[6] B. Cludovatz, A. Hohenwarter, D. Canoor, E.H. Chang, E.P. George, R.O. Ritchie, A fracture-resistant high-entropy alloy for cryogenic applications, Science 345 (2014) 1153–1158.
[7] H. Luo, Z. Li, D. Raabe, Hydrogen enhances strength and ductility of an equiatomic high-entropy alloy, Sci. Rep. 7 (2017) 9892.
[8] J.M. Park, J. Moon, J.W. Bae, J. Jung, S. Lee, H.S. Kim, Effect of annealing heat treatment on microstructural evolution and tensile behavior of $Al_{0.5}$CoCrFeMnNi high-entropy alloy, Mater. Sci. Eng. 728 (2018) 251–258.
[9] J.M. Park, J. Moon, J.W. Bae, D.H. Kim, Y.H. Jo, S. Lee, H.S. Kim, Role of BCC phase on tensile behavior of dual-phase $Al_{0.5}$CoCrFeMnNi high-entropy alloy at cryogenic temperature, Mater. Sci. Eng. 746 (2019) 443–447.
[10] Z. Lei, X. Liu, Y. Wu, H. Wang, S. Jiang, S. Wang, X. Hui, Y. Wu, B. Gault, P. Kontis, D. Raabe, L. Gu, Q. Zhang, H. Chen, H. Wang, J. Liu, K. An, Q. Zeng, T.G. Nieh, Z. Lu, Enhanced strength and ductility in a high-entropy alloy via ordered oxygen complex, Nature 563 (2018) 546–550.
[11] Z. Li, C. Tasan, H. Springer, B. Gault, D. Raabe, Interstitial atoms enable joint twinning and transformation induced plasticity in strong and ductile high-entropy alloys, Sci. Rep. 7 (2017), 40704.
[12] J.B. Seol, J.W. Bae, Z.M. Li, J.C. han, J.G. Kim, D. Raabe, H.S. Kim, Boron doped ultrastrong and ductile high-entropy alloys, Acta Mater. 151 (2018) 366–376.
[13] Z. Li, Interstitial equiatomic CoCrFeMnNi high-entropy alloys: carbon content, microstructure, and compositional homogeneity effects on deformation behavior, Acta Mater. 164 (2019) 400–412.
[14] J.Y. He, H. Wang, H.L. Huang, X.D. Xu, M.W. Chen, Y. Wu, X.J. Liu, T.G. Nieh, K. An, Z.P. Lu, A precipitation-hardened high-entropy alloy with outstanding tensile properties, Acta Mater. 102 (2016) 187–196.
[15] T. Yang, Y.L. Zhao, Y. Tong, Z.B. Jiao, J. Wei, J.X. Cai, X.D. Han, D. Chen, A. Hu, J. J. Kai, K. Lu, Y. Liu, C.T. Liu, Multicomponent intermetallic nanoparticles and superb mechanical behaviors of complex alloys, Science 362 (2018) 933–937.
[16] K. Ming, X. Bi, J. Wang, Precipitation strengthening of ductile $Cr_{15}Fe_{20}Co_{35}Ni_{20}Mo_{10}$ alloys, Scripta Mater. 137 (2017) 88–93.
[17] S. Fu, H. Bei, Y. Chen, T.K. Liu, D. Yu, K. An, Deformation mechanisms and work hardening behavior of transformation-induced plasticity high entropy alloys by in-situ neutron diffraction, Mater. Res. Lett. 6 (2018) 620–626.
[18] Z. Li, K.G. Pradeep, Y. Deng, D. Raabe, C.C. Tasan, Metastable high-entropy dual-phase alloys overcome the strength-ductility tradeoff, Nature 534 (2016) 227–230.
[19] D.X. Wei, X.Q. Li, W.C. Heng, Y. Koizumi, F. He, W.M. Choi, B.J. Lee, H.S. Kim, H. Kato, A. Chiba, Novel Co-rich high entropy alloys with superior tensile properties, Mater. Res. Lett. 7 (2019) 82–88.
[20] W. Lu, C.H. Liebscher, G. Dehm, D. Raabe, Z. Li, Bidirectional transformation enables hierarchical nanolaminate dual-phase high-entropy alloys, Adv. Mater. 30 (2018), 1804727.
[21] S.Y. Liu, Y.J. Wei, The Gaussian distribution of lattice size and atomic level heterogeneity in high entropy alloys, Extreme Mech Lett 11 (2017) 84–88.
[22] Z. Li, C.C. Tasan, K.G. Pradeep, D. Raabe, A TRIP-assisted dual-phase high-entropy alloy: grain size and phase fraction effects on deformation behavior, Acta Mater. 131 (2017) 323–335.
[23] J. Su, D. Raabe, Z. Li, Hierarchical microstructure design to tune the mechanical behavior of an interstitial TRIPTWIP high-entropy alloy, Acta Mater. 163 (2019) 40–54.
[24] Z.G. Zhu, X.H. An, W.J. Lu, Z.M. Li, F.L. Ng, X.Z. Liao, U. Ramamurty, S.M.L. Nai, J. Wei, Selective laser melting enabling the hierarchically heterogeneous microstructure and excellent mechanical properties in an interstitial solute strengthened high entropy alloy, Mater. Res. Lett. 7 (2019) 453–459.
[25] P. Niu, R. Li, K. Gan, T. Yuan, S. Xie, C. Chen, Microstructure, properties, and metallurgical defects of an equimolar CoCrNi medium entropy alloy additively manufactured by selective laser melting, Metall. Mater. Trans. 52 (2021) 753–766.
[26] L. Li, R. Li, T. Yuan, C. Chen, Z. Zhang, X. Li, Microstructures and tensile properties of a selective laser melted Al-Zn-Mg-Cu (Al7075) alloy by Si and Zr microalloying, Mater. Sci. Eng. 787 (2020), 139492.
[27] T. DebRoy, H.L. Wei, J.S. Zuback, T. Mukherjee, J.W. Elmer, J.O. Milewski, A. M. Beese, A. Wilson-Heid, A. De, W. Zhang, Additive manufacturing of metallic components - process, structure and properties, Prog. Mater. Sci. 92 (2018) 112–224.
[28] Z.G. Zhu, Q.B. Nguyen, F.L. Ng, X.H. An, X.Z. Liao, P.K. Liaw, S.M.L. Nai, J. Wei, Hierarchical microstructure and strengthening mechanisms of a CoCrFeMnNi high entropy alloy additively manufactured by selective laser melting, Scripta Mater. 154 (2018) 20–24.
[29] S.A. Khairallah, A.T. Anderson, A. Rubenchik, W.E. King, Laser powder-bed fusion additive manufacturing: physics of complex melt flow and formation mechanisms of pores, spatter, and denudation zones, Acta Mater. 108 (2016) 36–45.
[30] L. Thijs, K. Kempen, J.-P. Kruth, J. Van Humbeeck, Fine-structured aluminium products with controllable texture by selective laser melting of pre-alloyed AlSi10Mg powder, Acta Mater. 61 (2013) 1809–1819.
[31] C.Y. Yap, C.K. Chua, Z.L. Dong, Z.H. Liu, D.Q. Zhang, L.E. Loh, S.L. Sing, Review of selective laser melting: materials and applications, Appl. Phys. Rev. 2 (2015), 041101.

[32] L.N. Carter, C. Martin, P.J. Withers, M.M. Attallah, The influence of the laser scan strategy on grain structure and cracking behaviour in SLM powder-bed fabricated nickel superalloy, J. Alloys Compd. 615 (2014) 338–347.

[33] J.P. Kruth, G. Levy, F. Klocke, T. Childs, Consolidation phenomena in laser and powder-bed based layered manufacturing, CIRP Ann 56 (2007) 730–759.

[34] T. Trosch, J. Strößner, R. Völkl, U. Glatzel, Microstructure and mechanical properties of selective laser melted Inconel 718 compared to forging and casting, Mater. Lett. 164 (2016) 428–431.

[35] Y.C. Wang, L.M. Lei, L. Shi, H.Y. Wan, F. Liang, G.P. Zhang, Scanning strategy dependent tensile properties of selective laser melted GH4169, Mater. Sci. Eng. 788 (2020), 139616.

[36] J.M. Park, J. Choe, H.K. Park, S. Son, J. Jung, T.S. Kim, J.H. Yu, J.G. Kim, H.S. Kim, Synergetic strengthening of additively manufactured $(CoCrFeMnNi)_{99}C_1$ high-entropy alloy by heterogeneous anisotropic microstructure, Addit. Manuf. 35 (2020), 101333.

[37] Y. Chew, G.J. Bi, Z.G. Zhu, F.L. Ng, F. Weng, S.B. Liu, S.M.L. Nai, B.Y. Lee, Microstructure and enhanced strength of laser aided additive manufactured CoCrFeMnNi high entropy alloy, Mater. Sci. Eng. 744 (2019) 137–144.

[38] R. Li, P. Niu, T. Yuan, P. Cao, C. Chen, K. Zhou, Selective laser melting of an equiatomic CoCrFeMnNi high-entropy alloy: processability, non-equilibrium microstructure and mechanical property, J. Alloys Compd. 746 (2018) 125–134.

[39] Y.K. Kim, J. Choe, K.A. Lee, Selective laser melted equiatomic CoCrFeMnNi high-entropy alloy: microstructure, anisotropic mechanical response, and multiple strengthening mechanism, J. Alloys Compd. 805 (2019) 680–691.

[40] P. Niu, R. Li, S. Zhu, M. Wang, C. Chen, T. Yuan, Hot cracking, crystal orientation and compressive strength of an equimolar CoCrFeMnNi high-entropy alloy printed by selective laser melting, Opt Laser. Technol. 127 (2020), 106147.

[41] P.D. Niu, R.D. Li, T.C. Yuan, S.Y. Zhu, C. Chen, M.B. Wang, L. Huang, Microstructures and properties of an equimolar AlCoCrFeNi high entropy alloy printed by selective laser melting, Intermetallics 104 (2019) 24–32.

[42] C. Zhang, K. Feng, H. Kokawa, B. Han, Z. Li, Cracking mechanism and mechanical properties of selective laser melted CoCrFeMnNi high entropy alloy using different scanning strategies, Mater. Sci. Eng. 789 (2020), 139672.

[43] Z. Sun, X.P. Tan, M. Descoins, D. Mangelinck, S.B. Tor, C.S. Lim, Revealing hot tearing mechanism for an additively manufactured high-entropy alloy via selective laser melting, Scripta Mater. 168 (2019) 129–133.

[44] L. Guo, J. Gu, B. Gan, S. Ni, Z. Bi, Z. Wang, M. Song, Effect of elemental segregation and scanning strategy on the mechanical properties and hot cracking of a selective laser melted FeCoCrNiMn-(N, Si) high entropy alloy, J. Alloys Compd. 865 (2021), 158892.

[45] J.M. Park, J. Choe, J.G. Kim, J.W. Bae, J. Moon, S. Yang, K.T. Kim, J.H. Yu, H. S. Kim, Superior tensile properties of 1%C-CoCrFeMnNi high-entropy alloy additively manufactured by selective laser melting, Mater. Res. Lett. 8 (2019), 1638844.

[46] T.M. Rodgers, J.D. Madison, V. Tikare, Simulation of metal additive manufacturing microstructures using kinetic Monte Carlo, Comput. Mater. Sci. 135 (2017) 78–89.

[47] J. Akram, P. Chalavadi, D. Pal, B. Stucker, Understanding grain evolution in additive manufacturing through modeling, Addit. Manuf. 21 (2018) 255–268.

[48] O. Andreau, I. Koutiri, P. Peyre, J.-D. Penot, N. Saintier, E. Pessard, T.D. Terris, C. Dupuy, T. Baudin, Texture control of 316L parts by modulation of the melt pool morphology in selective laser melting, J. Mater. Process. Technol. 264 (2019) 21–31.

[49] J.J. Marattukalam, D. Karlsson, V. Pacheco, P. Beran, U. Wiklund, U. Jansson, B. Hjörvarsson, M. Sahlberg, The effect of laser scanning strategies on texture, mechanical properties, and site-specific grain orientation in selective laser melted 316L SS, Mater. Des. 193 (2020), 108852.

[50] S. Bahl, S. Mishra, K.U. Yaza, I.R. Kola, K. Chatterjee, S. Suwas, Non-equilibrium microstructure, crystallographic texture and morphological texture synergetically result in unusual mechanical properties of 3D printed 316L stainless steel, Addit. Manuf. 28 (2019) 65–77.

[51] P. Xue, L. Zhu, P. Xu, Y. Ren, B. Xin, S. Wang, Z. Yang, J. Ning, G. Meng, Z. Liu, CrCoNi medium-entropy alloy thin-walled parts manufactured by laser metal deposition: microstructure evolution and mechanical anisotropy, Mater. Sci. Eng. 817 (2021), 141306.

[52] R.N. Yellakara, Z. Wang, A three-dimensional dislocation dynamics study on the effects of grain size and shape on strengthening behavior of fcc Cu, Comput. Mater. Sci. 87 (2014) 253–259.

[53] W. Zhang, J. Shen, J.P. Oliveira, B.J. Kooi, Y.T. Pei, Crystallographic orientation-dependent deformation characteristics of additive manufactured interstitial-strengthened high entropy alloys, Scripta Mater. 222 (2023), 115049.

[54] W. Wu, R. Zhou, B. Wei, S. Ni, Y. Liu, M. Song, Nanosized precipitates and dislocation networks reinforced C-containing CoCrFeNi high-entropy alloy fabricated by selective laser melting, Mater. Char. 144 (2018) 605–610.

[55] J.M. Park, E.S. Kim, H. Kwon, P. Sathiyamoorthi, K.T. Kim, J.-H. Yu, H.S. Kim, Effect of heat treatment on microstructural heterogeneity and mechanical properties of 1%C-CoCrFeMnNi alloy fabricated by selective laser melting, Addit. Manuf. 47 (2021), 102283.

[56] P. Niu, R. Li, Z. Fan, T. Yuan, Z. Zhang, Additive manufacturing of TRIP-assisted dual-phases $Fe_{50}Mn_{30}Co_{10}Cr_{10}$ high-entropy alloy: microstructure evolution, mechanical properties and deformation mechanisms, Mater. Sci. Eng. 814 (2021), 141264.

[57] U.F. Kocks, H. Mecking, Physics and phenomenology of strain hardening: the FCC case, Prog. Mater. Sci. 48 (2003) 171–273.

[58] S.A.H. Motaman, F. Roters, C. Haase, Anisotropic polycrystal plasticity due to microstructural heterogeneity: a multi-scale experimental and numerical study on additively manufactured metallic materials, Acta Mater. 185 (2020) 340–369.

[59] Y.D. Im, K.H. Kim, K.H. Jung, Y.K. Lee, K.H. Song, Anisotropic mechanical behavior of additive manufactured AISI 316L steel, Metall. Mater. Trans. A 50 (2019) 2014. –2021.

[60] L. Thijs, M.L.M. Sistiaga, R. Wauthle, Q. Xie, J.-P. Kruth, J.V. Humbeeck, Strong morphological and crystallographic texture and resulting yield strength anisotropy in selective laser melted tantalum, Acta Mater. 61 (2013) 4657–4668.

[61] J.M. Jeon, J.M. Park, J.H. Yu, J.G. Kim, Y. Seong, S.H. Park, H.S. Kim, Effects of microstructure and internal defects on mechanical anisotropy and asymmetry of selective laser-melted 316L austenitic stainless steel, Mater. Sci. Eng. 763 (2019), 138152.

[62] B.H. Frodal, S. Thomesen, T. Børvik, O.S. Hopperstad, On the coupling of damage and single crystal plasticity for ductile polycrystalline materials, Int. J. Plast. 142 (2021), 102996.

[63] Y. Xia, K. Miao, H. Wu, L. Geng, C. Xu, C.H. Ku, G. Fan, Superior strength-ductility synergy of layered aluminum under uniaxial tensile loading: the roles of local stress state and local strain state, Int. J. Plast. 152 (2022), 103240.

[64] J.J. Jonas, L.S. Tóth, Modelling oriented nucleation and selective growth during dynamic recrystallization, Scripta Metall. Mater. 27 (1992) 1575–1580.

[65] J. Hirsch, E. Aryshesnkij, S. Konovalov, Slip system selection and Taylor factor evolution in FCC metals. Available at SSRN: https://doi.org/10.2139/ssrn.3618715

[66] L. Remy, A. Pineau, Twinning and strain-induced F.C.C. → H.C.P. transformation in the Fe-Mn-Cr-C system, Mater. Sci. Eng. 18 (1977) 99–107.

[67] B.C. De Cooman, Y. Estrin, S.K. Kim, Twinning-induced plasticity (TWIP) steels, Acta Mater. 142 (2018) 283–362.

[68] D. Wei, X. Li, J. Jiang, W. Heng, Y. Koizumi, W.M. Choi, B.J. Lee, H.S. Kim, H. Kato, A. Chiba, Novel Co-rich high performance twinning-induced plasticity (TWIP) and transformation-induced plasticity (TRIP) high-entropy alloys, Scripta Mater. 165 (2019) 39–43.

[69] G.B. Olson, M. Cohen, A general mechanism of martensitic nucleation: Part I. General concepts and the FCC → HCP transformation, Metall. Trans. A 7 (1976) 1897–1904.

[70] S. Huang, W. Li, S. Lu, F. Tian, J. Shen, E. Holmström, L. Vitos, Temperature dependent stacking fault energy of FeCrCoNiMn high entropy alloy, Scripta Mater. 108 (2015) 44–47.

[71] W.M. Choi, Y.H. Jo, S.S. Sohn, S. Lee, B.J. Lee, Understanding the physical metallurgy of the CoCrFeMnNi high-entropy alloy: an atomistic simulation study, npj Comput. Mater. 4 (2018) 1–9.

[72] A.J. Zaddach, C. Niu, C.C. Koch, D.L. Irving, Mechanical properties and stacking fault energies of NiFeCrCoMn high-entropy alloy, J. Occup. Med. 65 (2013) 1780–1789.

[73] S.F. Liu, Y. Wu, H.T. Wang, J.Y. He, J.B. Liu, C.X. Chen, X.J. Liu, H. Wang, Z.P. Lu, Stacking fault energy of face-centered-cubic high entropy alloys, Intermetallics 93 (2018) 269–273.

[74] Z. Wang, I. Baker, Z. Cai, S. Chen, J.D. Poplawsky, W. Guo, The effect of interstitial carbon on the mechanical properties and dislocation substructure evolution in Fe40.4Ni11.3Mn34.8Al7.5Cr6 high entropy alloys, Acta Mater. 120 (2016) 228–239.

[75] K. Yamanaka, M. Mori, A. Chiba, Origin of significant grain refinement in Co-Cr-Mo alloys without severe plastic deformation, Metall. Mater. Trans. A 43 (2012) 4875–4887.

[76] K. Yamanaka, M. Mori, A. Chiba, Nanoarchitectured Co–Cr–Mo orthopedic implant alloys: nitrogen-enhanced nanostructural evolution and its effect on phase stability, Acta Biomater. 9 (2013) 6259–6267.

[77] Y. Koizumi, S. Suzuki, K. Yamanaka, B.S. Lee, K. Sato, Y. Li, S. Kurosu, H. Matsumoto, A. Chiba, Strain-induced martensitic transformation near twin boundaries in a biomedical Co–Cr–Mo alloy with negative stacking fault energy, Acta Mater. 61 (2013) 1648–1661.

[78] D. Wei, Y. Koizumi, T. Takashima, M. Nagasako, A. Chiba, Fatigue improvement of electron beam melting-fabricated biomedical Co–Cr–Mo alloy by accessible heat treatment, Mater. Res. Lett. 6 (2018) 93–99.

[79] K. Rajan, J.B. Vander Sande, Room temperature strengthening mechanisms in a Co-Cr-Mo-C alloy, J. Mater. Sci. 17 (1982) 769–778.

[80] E. Ma, X. Wu, Tailoring heterogeneities in high-entropy alloys to promote strength–ductility synergy, Nat. Commun. 10 (2019) 5623.

[81] M. Laleh, A.E. Hughes, S. Yang, J. Li, W. Xu, I. Gibson, M.Y. Tan, Two and three-dimensional characterisation of localised corrosion affected by lack-of-fusion pores in 316L stainless steel produced by selective laser melting, Corrosion Sci. 165 (2020), 108394.

[82] S. Wen, S. Li, Q. Wei, C. Yan, S. Zhang, Y. Shi, Effect of molten pool boundaries on the mechanical properties of selective laser melting parts, J. Mater. Process. Technol. 214 (2014) 2660–2667.

[83] Z. Xu, Q. Wang, X. Wang, C. Tan, M. Guo, P. Gao, High cycle fatigue performance of AlSi10Mg alloy produced by selective laser melting, Mech. Mater. 148 (2020), 103499.